Highlights of Spanish Astrophysics XII, Proceedings of the XVI Scientific Meeting of the Spanish Astronomical Society held on July 15 - 19, 2024, in Granada, Spain. M. Manteiga, F. González Galindo, A. Labiano Ortega, M. Martínez González, N. Rea, M. Romero Gómez, A. Ulla Miguel, G. Yepes, C. Rodríguez López, A. Gómez García and C. Dafonte (eds.), 2025

Scientific forecasts for cluster cosmology with a projected 4-band millimetre camera at the 30-m IRAM telescope

Fernández-Torreiro, M.[1], Chérouvrier, D.[1], Macías-Pérez, J.F.[1] and F.X. Désert[2]

[1] Laboratoire de Physique Subatomique et de Cosmologie, Université Grenoble Alpes, CNRS/IN2P3, 53, avenue des Martyrs, Grenoble, France
[2] Univ. Grenoble Alpes, CNRS, IPAG, F-38000 Grenoble, France

Abstract

The Sunyaev-Zel'dovich effect has been a powerful cosmological probe for almost 30 years now, and significant progresses on its observation with arcminute resolution telescopes has been achieved in the last 15 years. In this work, we build upon the NIKA2 legacy to propose a new, updated version of the camera. This new instrument would have two additional frequency bands (at 90/230 GHz) and would feature a larger field-of-view of $10'$, thus boosting its mapping speed. We present the expected performance after such improvements, both for the observation of individual galaxy clusters and for blind searches of clusters. The improved sensitivity greatly eases the detection of the kinematic Sunyaev-Zel'dovich effect, and in the latter case the number of expected galaxy clusters detected grows by a factor 3.

1 Introduction

Galaxy clusters (GC) are the largest gravitationally bound objects in the Universe. They are made of ($\sim 85\%$) dark matter, gas in the intracluster medium (ICM, $\sim 12\%$) and galaxies ($\sim 3\%$). The inverse Comptonization that cosmic microwave background (CMB) photons undergo when crossing this hot ($T_e \geq 10^6\,\mathrm{K}$) ICM receives the name of Sunyaev-Zel'dovich (SZ) effect [1]. This effect implies a modification of the CMB blackbody spectrum, with an excess/defect of signal above/below 217 GHz.

The SZ effect has been for a while now a powerful astrophysical probe to detect GC. It is also a complementary test to optical surveys, as these trace the actual distributions described by the galaxies, while the SZ effect traces the distribution of the ICM, which also emits in X-ray wavelengths. Because of the particular spectrum behavior of the SZ effect, it can be easily separated from other CMB foregrounds, and its angular scales are well below those from primary CMB anisotropies ($\leq 10'$ vs. $\sim 1°$). Significant efforts have been devoted to the detection, observation and analysis of GC at $\geq 1'$ resolutions in the last 20 years, both from satellite [2] and ground-based [3, 4] experiments.

We can identify two components to the SZ effect: the first one, which matches the description provided above, is known as the thermal SZ effect. The measured variation of the CMB spectrum is described as:

$$\Delta I_\nu^{\mathrm{tSZ}} = I(x) \times y_{\mathrm{tSZ}} \times f_{\mathrm{tSZ}}(x) \left[1 + \delta_{\mathrm{tSZ}}(x, T_e)\right]; \quad \text{where} \quad y_{\mathrm{tSZ}} = \frac{k_B \overline{T_e}}{m_e c^2} \int \tau_e dl \tag{1}$$

with $I(x)$ being the CMB intensity, f_{tSZ} being the spectral dependence of the thermal SZ effect (with opposite sign below and above 217 GHz) and $\delta_{\mathrm{tSZ}}(x, T_e)$ being the further relativistic corrections induced by the high electronic temperature of the ICM. The optical depth $\tau = \int \tau_e dl$ will be used as the effective varying amplitude of the thermal SZ throughout this paper.

The second SZ component is known as the kinematic SZ effect, and it consists of the deviations from the CMB blackbody spectrum due to the GC peculiar velocity with respect to the CMB reference frame. In this case, the spectrum shape is the same as the one from the CMB blackbody. This, together with the limited velocities the GC can achieve ($\leq 3000\,\mathrm{km\,s^{-1}}$) turn this effect subdominant and more difficult to detect than the thermal one:

$$\Delta I_\nu^{\mathrm{kSZ}} = I(x) \times y_{\mathrm{kSZ}} \times [1 + \delta_{\mathrm{kSZ}}(x, T_e, v_z)]; \quad \text{where} \quad y_{\mathrm{kSZ}} = -\frac{v_z}{c} \int \tau_e dl \tag{2}$$

In this work, we present the forecasted performance for a possible successor of the NIKA2 camera, which has been observing GC with $< 1'$ angular resolutions since 2015. We particularly highlight the expected improvement on the detection of the kinematic SZ effect component, and that achieved when performing blind searches of GC.

2 The IRAM 30-m telescope and the NIKA2 instrument. Proposed upgrade

The Institut de radioastronomie millimétrique (IRAM) operates the 30-m antenna located in Pico Veleta, Granada, Spain. It is located at an altitude of 2850 metres, with typical precipitable water vapour (PWV) values of 2–6 mm [5], ideal for millimetre observations.

The NIKA2 instrument consists of a dual-band millimetre continuum camera with almost 2900 kinetic inductance detectors (KID, [6]). Its two frequency bands, observing at 150 and 260 GHz, allow for a clean separation between the emission from GC due to the SZ effect and that from point sources. Also, the high angular resolution of the telescope at such frequencies (at the 10–20$''$ level) resolves the SZ imprint from the larger, more important primary anisotropies of the CMB. A complete description of the NIKA2 instrument is available in [7].

We propose to add two additional frequency bands at 90 and 230 GHz in a new iteration of the NIKA2 camera. In addition, we propose to increase the number of detectors so the effective field-of-view (FoV) increases from $6.5'$ to $10'$. This increases the mapping speed of

Table 1: Comparison between NIKA2 performance and that expected for the new camera. Notice how the improvement for the latter comes from the larger FoV and therefore the increased mapping speed ($M_s \propto d^2_{\mathrm{FoV}}$), not due to a better single KID performance.

	NIKA2		New camera			
Field-of-view (arcminutes)	6.5		10			
Reference frequencies (GHz)	150	260	90	150	230	260
M_s (arcmin^2 mJy^{-2} h^{-1})	1388 ± 174	111 ± 11	3331	3331	266	266

the instrument by a factor 2.4. We have assumed that this factor is entirely translated into a similar decrease of the noise from the final maps, although the actual improvement will be marginally lower due to the observing strategy of the telescope. The precise numbers, together with those from NIKA2 used for comparison purposes, are shown in Table 1.

3 Forecasts for detections of individual GCs

We first estimate the performance of the new instrument when observing spatially resolved, individual GC. We use the *minot* software [8] to simulate the pressure, density and temperature profiles of the GC. We assume the universal pressure profile from REXCESS data [9] and spherical symmetry. We then integrate the parameters along the line-of-sight in order to obtain the SZ amplitude maps (y_{tSZ} and y_{kSZ} from Eqs. 1 and 2, respectively).

From these two, together with realistic realizations of the white noise component as presented in Table 1, we build the maps for the two instruments at their respective frequencies. We show examples for both instruments in Fig. 1 for a GC with $M_{500} = 7 \cdot 10^{14}\, M_\odot$, $z = 0.7$ and $v_{\mathrm{LOS}} = -1000\,\mathrm{km\,s^{-1}}$. Finally, we perform aperture photometry similarly to previous works (e.g. [10]), i.e. as the difference between the mean signal within a circle (that we defined with radius $r = 1.5\theta_{500}$) and the median within an external region (that we defined as the rest of our simulation). We fit the derived data with a Maximum Likelihood Estimator (MLE) using a Markov Chain Monte Carlo (MCMC like in for example, [11]) to a combination of thermal and kinematic SZ effects. We show in Fig. 2 the posterior distributions for the amplitudes of the two SZ components, parametrized by τ (for the thermal and kinematic components) and $\beta_c = v_z/c$ (for the kinematic one).

The improvement achieved with respect to NIKA2 is immediately evident. While NIKA2 is not capable of disentangling the thermal and kinematic components with enough significance, the new iteration achieves a 3σ detection of the latter. We generate a M_{500} - v_{LOS} - z grid in order to study this improvement with varying properties of the GC. The results imply that the new camera would be able to recover the kinematic SZ from GC with intermidate-to-high masses and redshifts ($M_{500} > 5 \cdot 10^{14} M_\odot$, $z > 0.3$), while for NIKA2 either high masses ($M_{500} > 8 \cdot 10^{14} M_\odot$) or velocities ($v_{\mathrm{LOS}} \geq 3000\,\mathrm{km\,s^{-1}}$) are required.

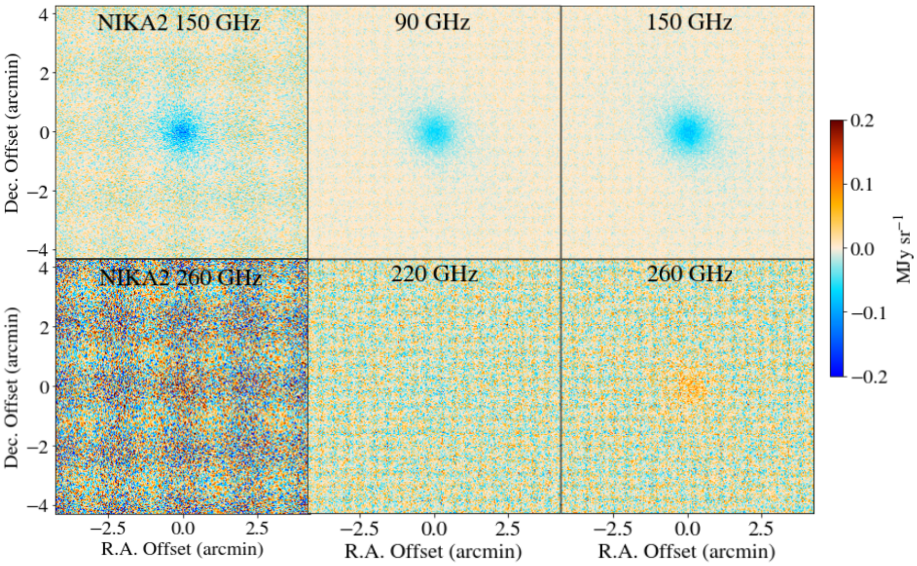

Figure 1: Simulations ($t_{\rm obs} = 5\,$hours) for a GC with $M_{500} = 7 \cdot 10^{14}\,M_\odot$, $z = 0.7$ and $v_{\rm LOS} = -1000\,{\rm km}^{-1}$ observed by NIKA2 (left panels) and our proposed new iteration. We see the improvement because of the lower white noise component from the latter. The apparent square pattern is an artifact of our visualization software.

4 Blind detections of GC on extended fields

Now, we generate mock catalogues of GC with $0 < z < 3$ and $2 \cdot 10^{13} < M_{500}(M_\odot) < 3 \cdot 10^{15}$ following the realistic mass function from [12]. In this case, we consider only the thermal SZ component, as it is responsible for most of the SZ signal and thus will be the limiting factor when performing blind searches of GC. We simulate the emission and integrate it along the line-of-sight in the same way as in the previous chapter, but now for all the GC in the catalogues. We add a white noise component consistent with the values given in Section 2. We then obtain a set of maps where we ran a match-filter search [13, 14] in order to detect the GC, and compare our results with the input values from the catalogue.

We show in Fig. 3 the comparison between the simulated maps at 150 GHz with NIKA2 and the new camera. We detect 13 GC in the NIKA2 map, while this number increases by a factor 3, up to 42, for the latter. The purity is also better, as we only have two false detections in both cases. When increasing the number of mock catalogues to $N_{sims} = 100$ we detect a similar behavior, with the real detections increasing to ~ 1100 and ~ 3500 for NIKA2 and the proposed new camera, respectively. These are 6% and 19% of the sources in the input catalogues. This completeness improvement is located at lower masses and redshifts, mostly below $10^{14}\,M_\odot$. The purity in the new camera simulation observations reaches $> 95\%$, although it was already quite good for NIKA2, being at $> 85\%$ level, both when fixig $SNR = 4$ as the threshold for detection.

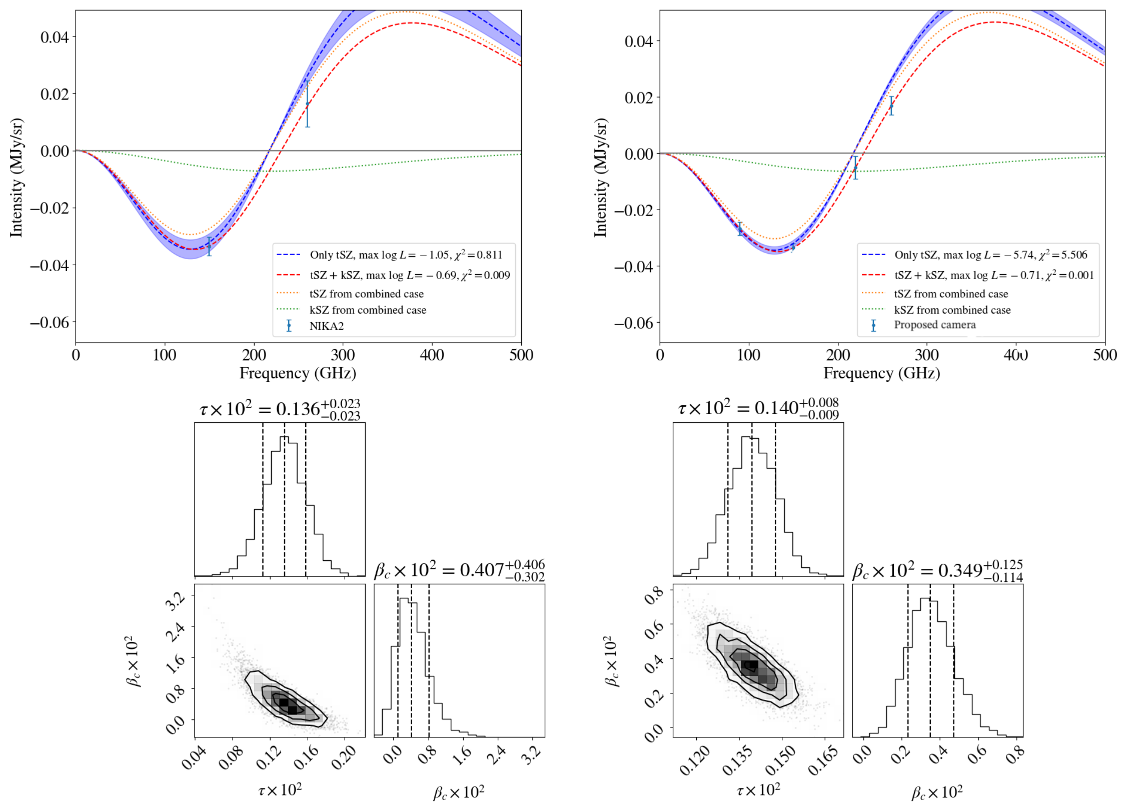

Figure 2: Top: spectral energy distributions (SED) obtained by NIKA2 (left) and our proposed iteration (right) with the best fit to the data considering thermal and kinematic SZ effects. Bottom: posterior distributions for the amplitudes of the two components obtained by NIKA2 (left, with the kinematic amplitude being consistent with zero) and the proposed iteration (right). The latter shows an almost 3σ detection of the kinematic component, consistent with our input value and a significant improvement with respect to NIKA2.

5 Conclusions

In this work we have presented the expected performance improvement that an upgraded NIKA2-like experiment would achieve by adding two new frequency bands and a bigger FoV. Adding the first one improves the separation between the thermal and kinematic components of the SZ effect when performing observations of single GC. The second one plays an important role on such improvement too, but it also increases by a factor of 3 the number of GC detected on blind searches on the sky. We leave for future work the discussion on the improvement of the reconstruction of the relativistic corrections to the thermal SZ component, together with the possible improvements on the blind search analyses achieved by the combination of multifrequency data.

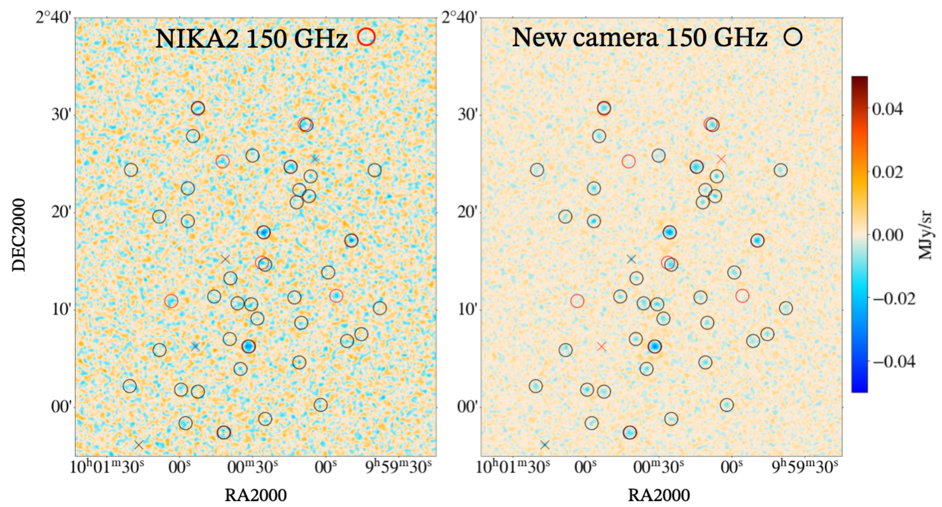

Figure 3: Example of a simulation for a COSMOS-like [15] field populated by a mock catalogue of GC. Left: the field as observed by NIKA2 150 GHz band; right: the field as observed by the new camera at the same frequency. Circles in red and black represent the real detections obtained by the match filter on NIKA2 maps and those obtained by the new proposed camera, respectively. Crosses represent the false detections, with the same color scheme.

References

[1] Sunyaev, R. A. & Zeldovich, Y. B. 1972, Comments on Astrophysics and Space Physics, 4, 173

[2] Planck Collaboration, Ade, P. A. R., Aghanim, N., et al. 2014, A&A, 571, A20

[3] Hilton, M., Sifón, C., Naess, S., et al. 2021, ApJS, 253, 3

[4] Bleem, L. E., Klein, M., Abbot, T. M. C., et al. 2024, The Open Journal of Astrophysics, 7, 13

[5] Raymond, A. W., Palumbo, D., Paine, S. N., et al. 2021, ApJS, 253, 5

[6] Zmuidzinas, J. 2012, Annual Review of Condensed Matter, 3, 169

[7] Perotto, L., Ponthieu, N., Macías-Pérez, J. F., et al. 2020, A&A, 637, A71

[8] Adam, R., Goksu, H., Leingärtner-Goth, A., et al. 2020, A&A, 644, A70

[9] Arnaud, M., Pratt, G. W., Piffaretti, R., et al. 2010, A&A, 517, A92

[10] Fernández-Torreiro, M., Génova-Santos, R. T., Rubiño-Martín, J. A., et al. 2024, MNRAS, 527, 11945

[11] Fernández-Torreiro, M., Rubiño-Martín, J. A., López-Caraballo, C. H., et al. 2023, MNRAS, 526, 1343

[12] Tinker, J., Kravtsov, A. V., Klypin, A., et al. 2008, ApJ, 688, 709

[13] Melin, J.-B., Bartlett, J. G., & Delabrouille, J. 2006, A&A, 459, 341

[14] Erler, J., Ramos-Ceja, M. E., Basu, K., et al. 2019, MNRAS, 484, 1988. doi:10.1093/mnras/stz101

[15] Bing, L., Béthermin, M., Lagache, G., et al. 2023, A&A, 677, A66. doi:10.1051/0004-6361/202346579